Daytime aspect camera for balloon altitudes

Kurt L. Dietz
Brian D. Ramsey
Cheryl D. Alexander
Jeff A. Apple
NASA/Marshall Space Flight Center
Science Directorate
Huntsville, Alabama 35812

Kajal K. Ghosh
University Space Research Associates
Huntsville, Alabama

Wesley R. Swift
Raytheon ITSS
Huntsville, Alabama

Abstract. We have designed, built, and flight-tested a new star camera for daytime guiding of pointed balloon-borne experiments at altitudes around 40 km. The camera and lens are commercially available, off-the-shelf components, but require a custom-built baffle to reduce stray light, especially near the sunlit limb of the balloon. This new camera, which operates in the 600- to 1000-nm region of the spectrum, successfully provides daytime aspect information of ~10 arcsec resolution for two distinct star fields near the galactic plane. The detected scattered-light backgrounds show good agreement with the Air Force MODTRAN models, but the daytime stellar magnitude limit was lower than expected due to longitudinal chromatic aberration in the lens. Replacing the commercial lens with a custom-built lens should allow the system to track stars in any arbitrary area of the sky during the daytime. [DOI: 10.1117/1.1501566]

Paper 010428 received Nov. 26, 2001; revised manuscript received Feb. 26, 2002; accepted for publication Mar. 5, 2002.

1 Background

Daytime aspect systems have presented a continuing challenge for pointed, balloon-borne experiments. Typically,[1] these experiments have utilized a sun sensor during the day and a star camera during the night, which is far from ideal. Not only does a second, nonredundant aspect system increase the expense, complexity, mass, and power consumption of a balloon-borne payload, but a sun sensor also has limited precision (~1 arcmin, which degrades with increasing solar elevation angle), and cannot be used when the sun rises above ~65-deg elevation and is occulted by the balloon. For a new generation of hard x-ray focusing telescopes, such as the High Energy Replicated Optics (HERO)[2] experiment being developed at the Marshall Space Flight Center (MSFC), the aspect information from a sun sensor is insufficiently precise to facilitate useful science. The relatively narrow field-of-view of the x-ray optics necessitates a pointing precision of 0.5-1 arcmin, and the high resolution (~15 arcsec half power diameter for the HERO optics) requires an attitude knowledge of 7 to 8 arcsec to avoid compromising the resolution of the mirrors. Since constraints on balloon launch times and flight windows often necessitate daytime observations, some system must be found to provide high-precision aspect information for these experiments during daylight hours.

A single star-camera-based system for both day and night observations is the preferred solution, but it faces serious obstacles. Not only must a daytime star camera contend with scattered sunlight from the residual atmosphere above a typical 40-km balloon float altitude, but also with the sunlight scattered off the surface of the balloon. One solution is to operate the camera in the infrared, in the window around 2 μm where the scattered daylight background is relatively low, but this approach is quite expensive. We have chosen a more affordable solution for the day/night aspect camera designed for the HERO experiment, which is to operate at red to near-infrared wavelengths using a carefully chosen, commercially available lens and CCD camera and a custom-built baffle. We present details of the camera design and the daytime performance of the system measured during two flights from Fort Sumner, New Mexico.

2 Implementation

As detailed in a preflight publication,[3] we began the design of our daylight aspect camera with trade studies using the Air Force Geophysics Laboratory's MODTRAN atmospheric radiation model and numerical star count models for the B, V, R and I filter bands developed for the 2MASS mission. We attempted to maximize the number of guide stars available in a daylight camera field in three ways: 1. by reducing the solid angle of each CCD pixel on the sky to reduce the amount of diffuse scattered light in each pixel; 2. by maintaining a reasonably large field of view to maximize the number of stars available to the guide camera; and 3. by identifying a wavelength region that gives relatively low sky brightness and high average star brightness. The camera choice is further constrained by the stability of the inertial guidance system. To meet the ~10-arcsec pointing knowledge requirement, our camera must be limited to exposures of 0.25 sec or less to avoid significant trailing of the star images.

We immediately identified the red portion of the spectrum as the most promising to reduce sky brightness relative to star brightness, but we did not settle immediately on a specific filter. Instead, since a wide variety of quality red filters could be purchased at trivial cost, we purchased several low-pass filters ranging from medium yellow to near infrared for later tests to determine which would give the best signal-to-noise ratio for our given exposure time constraints.

Next, we balanced the small pixel size and large field of view by careful selection of a commercial CCD camera and lens. The digital camera is a Photometrics SenSys, which is based on a thermoelectrically cooled Kodak 1401e CCD consisting of 6.8-μm-square pixels in a 1317×1035 array.

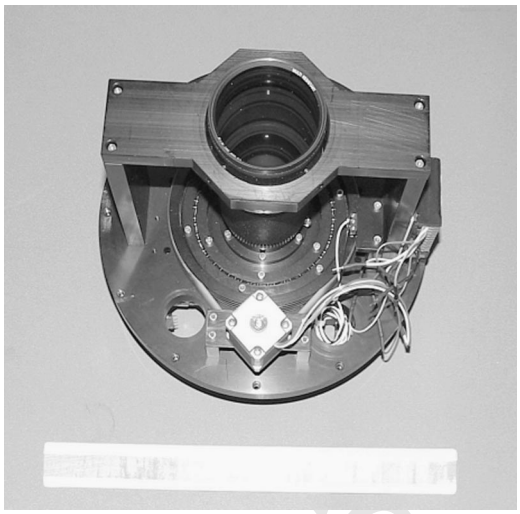

Fig. 1 Star camera unit mounted in focusing assembly.

This CCD combines high quantum efficiency with extended red light response, and comes in a relatively compact and lightweight camera package with a mechanical shutter offering exposures from 1 ms up to several minutes. We matched this camera with a 180-mm Nikon IF ED lens, which, at the minimum focal ratio of f/2.8, gives a diffraction-limited spot size (at a representative wavelength of 650 nm) of around 5 μm (2.5 μm radius), which is smaller than the CCD pixel size. This combination of lens and CCD gives a pixel size, projected on the sky, of 7.8 $\times$7.8 arcsec and a field of view of 2.84$\times$2.23 deg.

Our camera and lens selection was based on sensitivity calculations that assumed the light from each star would be spread into a maximum of four CCD pixels only, which can occur if the center of even a diffraction-limited star image is at the corner between four pixels. In this case, a diffraction-limited star image cannot be distinguished from larger images, up to the maximum allowable radius of 6.8 μm radius. Any further spreading due to poor focus will only reduce the signal-to-noise ratio in the pixels and degrade the sensitivity; therefore, accurate focus is vitally important to the sensitivity of the aspect system. Because temperature changes, atmospheric pressure, and disturbances at launch could all affect the focus of the camera lens after launch, we designed the camera to allow adjustment of the focus during flight.

The entire aspect system is implemented in a modular fashion. The CCD camera, lens, filter, focusing frame, and focus motor form the innermost camera unit, as shown in Fig. 1. The focus motor is a stepper motor, which has been geared to give 4000 steps per revolution, or about 2200 steps over the entire focus range of the lens. It is controlled by a separate unit (not shown), which, in turn, has a serial link that can be connected to a computer to read and control the focus position of the camera lens. The camera itself connects through a SCSI cable to a PCI-bus digital interface board supplied with the camera.

The camera unit could be used on the ground as pictured (with the addition of the motor controller), but was repackaged for flight in an outer pressure chamber with a glass window for the camera to view through. This combined module, known as the camera tank, is pressurized at one atmosphere for flight, allowing passive cooling of the electronics and ensuring a good thermal and pressure environment for free movement of the lens components. Mechanically, the bottom of the camera tank is bolted onto the rear bulkhead of the optical bench, next to the x-ray detectors. Electrically, it is powered through the computer system used to control the focus motors and process the aspect images.

The preflight publication[3] also identified the need for a baffle tube to reduce stray light directly from the sun and from the bright sky and the illuminated balloon, which otherwise might be a significant source of background in the aspect images. Since the x-ray transmittance of the atmosphere is greatest near zenith, we wanted to point as close to zenith, and therefore to the limb of the balloon, as possible. Given the constraints of the gondola mechanical clearances, we were able to design a baffle to allow pointing to within 5 deg of the balloon limb. Light from the farther off axis is forced to undergo reflection from at least four internal surfaces before reaching the focal plane of the CCD. The resulting baffle is 2.86 m in length, contains nine internal baffle apertures to reduce internal reflections, and bolts to the front of the camera tank. All the internal surfaces of the baffle are coated with a silicone-based, nonspecular black coating having a reflectivity of 2% at 700 nm to further reduce the amount of stray light reaching the camera, giving a minimum (four surface reflection) attenuation of $1/(0.02)^4 = 6.2\times10^6$ for photons outside the field of view.

The remaining module of the aspect system is the aspect computer, which is built around a 233-MHz Intel Pentium MMX-based single-board computer and mounts on the balloon gondola's elevation flange away from the optical bench. The aspect computer system contains the digital interface board to the camera, the serial port to the focus motor controller, and a network card to connect to the rest of the gondola control system. It is responsible for processing the camera images during both star-tracking and focusing operations, and for storing the images on a hard disk drive for further examination on the ground. The aspect computer is also contained in a pressure vessel pressurized to one atmosphere to allow proper operation of the hard drive and provide passive cooling for the electronics.

Aspect operations are split into two independent modes: a star tracking mode and an autofocus mode. In both cases, the readout of the camera is a significant source of the image processing time. The digital camera provides onboard 12-bit digitization of the pixel data at a rate of 1 MHz. This implies about 1.4 sec for an entire image to be read and transferred to the aspect computer, as in star tracking operations, and about 0.35 sec for the central quadrant of the image, as in autofocus operations.

After reading the entire CCD frame from the camera, the star-tracking software scans the image to find pixel values greater than five sigma above the background level, combines contiguous significant pixels into a single ''blob,'' and accepts only those blobs that have a total count greater than 20 sigma above the background. These blobs are then identified as stars by finding their centroids, calculating their relative separations, and comparing these separations with those found between objects in the target field of the

star catalog (the epoch 2000.0 Hipparcos star catalog,[4] available on-line). Given at least four valid, identified stars, this method can reliably produce the altitude, elevation, and rotational offsets of the image center from the target coordinates. Each image takes an average of ~1 sec to process, in addition to the readout time of the camera.

In autofocus mode, the central quadrant of the CCD frame is processed to calculate the sum of the squares of the differences between each pixel and one selected neighboring pixel. This focus figure is calculated for a series of images taken at periodic stepper-motor positions and used as the weight in a weighted mean estimate of the best focus position. This process is then repeated in a limited range around the estimated position using smaller steps. Our system uses three such stages, the first covering the entire focal range with 100-step intervals, the second covering 200 steps using 10-step intervals, and the final stage covering 20 steps using 1-step intervals. The total time to focus the camera is on the order of 3 min.

3 Predictions for Flight

Although our initial study indicated the red region of the spectrum as the most useful for daytime star-field imaging, we did not immediately select an optimum filter for use. A more detailed model of the sky background, breaking down the 600- to 1000-nm region of the spectrum into 50-nm bands, was needed. In addition, we wanted to investigate the effect of other factors such as cloud cover and aerosol contaminants on the background. These modeled background levels can then be added to nighttime images of target x-ray-source star fields taken from the ground through various promising filters to give us the best possible prediction of in-flight filter performance, which allows us to choose the best filter and to predict the in-flight background and sensitivity.

First, we examined the effect of aerosol pollutants and cloud cover on the daytime scattered light background. We ran the MODTRAN simulation software for two sets of cases, the first with no cloud cover or aerosol content, and the second with a cumulus cloud cover to 3-km altitude and aerosol pollutants giving a visibility of 50 km at sealevel. Each case depicted the expected sky background at a float altitude of 40 km and a wavelength of 0.6 μm (600 nm) as a function of view zenith angle (VZA) with the sun at two different positions: at 70-deg zenith angle (SZA = 70 deg) with the viewing azimuth 180 deg from that of the sun [sun azimuth angle (SAA) = 180 deg], and at 70-deg zenith angle (SZA = 70 deg) and viewing azimuth equal to that of the sun (SAA = 0 deg). These illustrative simulation results are shown in Fig. 2.

Figure 2(a) shows the view away from the sun, while Fig. 2(b) shows the view toward the sun. In both figures, the diamond-shaped points indicate the background without clouds or pollutants, and the square-shaped points indicate the background with cumulus cloud cover and aerosol pollutants present. As is obvious in both plots, the presence of the clouds and aerosols adds to the atmospheric scattering, and although this produces only a small increase in total sky radiance in the antisun direction [Fig. 2(a)], its effect is considerable in the forward direction close to the sun [Fig. 2(b)]. Since the visibility at the principal balloon launch site, in Fort Sumner, New Mexico, is typically around 80 km and cloudless conditions are common, we predict that the simpler model without clouds or aerosols will be the most accurate prediction of our in-flight sensitivity. However, because some amount of pollution and cloud cover at levels too low to be modeled is likely, we expect the observed background to be slightly higher than our chosen model, and the sensitivity therefore slightly lower.

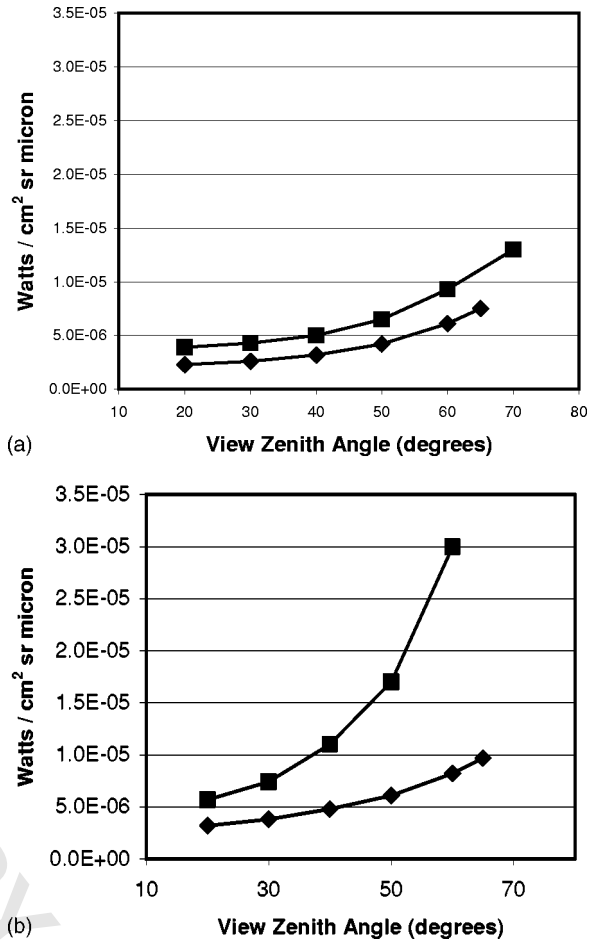

Fig. 2 MODTRAN-simulated daytime sky brightness at 0.6 μm as a function of view angle for two sun positions. Altitude is 40 km, diamonds represent backgrounds without clouds or aerosols, squares represent backgrounds with cumulus cloud cover and aerosol pollutants giving 50-km visibility at sea level. (a) is with the sun at zenith angle 70 deg, and the viewing azimuth 180 deg away from the sun. (b) is with the sun at zenith angle 70 deg and the viewing azimuth in the same direction as the sun (see text.)

Figure 3 shows the spectral distribution of the MODTRAN-derived sky background for a typical pointing direction from Fig. 2(a) (SZA = 0, VZA = 50). This spectral distribution is relatively insensitive to sun or view angle, which facilitates comparison between backgrounds of different illumination conditions.

To calculate the expected sensitivity in a given waveband for a particular target object and time of observation, we fold the appropriate model background with the camera quantum efficiency and the filter, lens, and tank window transmittances to give an expected number of electrons per CCD pixel. We then compare that count with the expected electron count for a zero magnitude star of spectral type G2, also folded through the camera and optics, and then

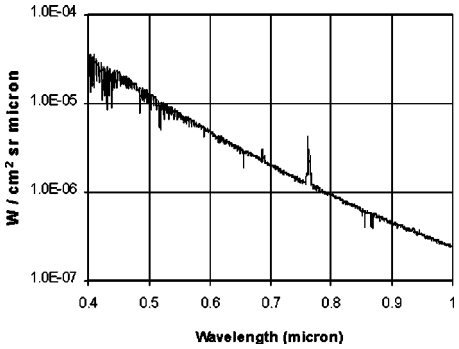

Fig. 3 MODTRAN-simulated spectrum of the daytime sky background at 40-km altitude, calculated for 0-deg solar zenith angle and 50-deg viewing zenith angle (see text).

scale the star intensity to give an appropriate detection significance. As a starting point we spread the star image over four pixels and ask that each be five sigma above the background count level.

Tables 1 and 2 show this process for a typical fall observation from Fort Sumner, New Mexico. The Crab Nebula, one of the brightest cosmic x-ray sources at balloon altitudes, is observed at 15:00 Universal Time on September 20, when its zenith angle is 33 deg. At this time the sun is at a zenith angle of 67 deg and at an azimuth 140 deg around from the Crab. The altitude is taken to be 40 km.

For a 0.25-sec integration, Table 1 shows that the total sky background in our camera will be $\sim 5\times 10^3$ electrons per pixel, with a standard deviation of 70 electrons. Note that the well depth in our chosen CCD is 40,000 electrons, so that in a 0.25-sec integration the wells are only 12% full. With a background standard deviation of 70 electrons, we would need a signal of ~ 350 electrons per pixel for a five sigma detection. If we assume that a star image is spread over four pixels, and that we want five sigma in each of these to avoid unambiguous detections, we then require a total of 1.4×10^3 electrons from the star for a significant detection in this time. Table 2 shows that a zero magnitude G2-type star gives 3.25×10^7 electrons/sec or $\sim 8.1\times 10^6$ electrons in 0.25 sec. Thus the limiting system magnitude would be $\sim \log(8.1\times 10^6/1.4\times 10^3)/\log(2.5119)\sim 9.4$. The visual magnitude is used here, rather than a red magnitude, as the star catalogue we use gives the visual magnitudes only.

A limiting sensitivity of ninth magnitude, as derived before, will give a comfortably large number of daytime stars for guidance, particularly in the galactic plane where the Crab resides. Looking at a star map of the Crab region, we can count 15 stars, ninth magnitude or brighter, that would be in the camera's field of view. Even 60 deg out of the galactic plane, we can still expect at least one star per square degree,[5] or around six stars visible in the field.

To select an optimum filter for use in flight, we tested a range of filters with different ''cut-on'' wavelengths on the Crab Nebula field, which was the most important target field in terms of testing the x-ray optics under development. For each filter, we took a 0.25-sec nighttime image from the ground at Huntsville using a duplicate camera and lens to that used in flight. We then modeled the daylight background expected at the float altitude of 40 km for the same filter and exposure, and uniformly added that background (plus simulated statistical count noise) to each pixel in the image. Note that the backgrounds used in this table assume a different (less favorable) viewing geometry from those in Table 1, and the B+W 090 filter value is consequently higher than the corresponding background derived in that table. We then used our flight aspect solution software to

Table 1 MODTRAN simulated daytime sky background rate, per pixel, in the star camera (see text).

Sterad/pixel	1.43E−09								
Lens diam (cm)	6.43								
Wavelength (micron)	W/ cm2 sr micron	W/micron	W over (50 nm) band	Mean # photons/ W	Photons/s over band	Filter B+W 090 and lens	Window trans.	CCD QE	CCD electrons/s
1	1.40E−07	6.50E−15	3.25E−16	5.04E+18	1.64E+03	0.46	0.918	0.06	4.15E+01
0.95	1.90E−07	8.82E−15	4.41E−16	4.79E+18	2.11E+03	0.51	0.918	0.1	9.89E+01
0.9	2.60E−07	1.21E−14	6.04E−16	4.54E+18	2.74E+03	0.56	0.918	0.2	2.81E+02
0.85	3.70E−07	1.72E−14	8.59E−16	4.28E+18	3.68E+03	0.64	0.917	0.3	6.48E+02
0.8	5.30E−07	2.46E−14	1.23E−15	4.03E+18	4.96E+03	0.73	0.917	0.32	1.06E+03
0.75	7.80E−07	3.62E−14	1.81E−15	3.78E+18	6.85E+03	0.79	0.917	0.47	2.33E+03
0.7	1.20E−06	5.57E−14	2.79E−15	3.53E+18	9.83E+03	0.84	0.917	0.51	3.86E+03
0.65	1.80E−06	8.36E−14	4.18E−15	3.28E+18	1.37E+04	0.84	0.916	0.6	6.32E+03
0.6	2.80E−06	1.30E−13	6.50E−15	3.02E+18	1.97E+04	0.45	0.916	0.6	4.86E+03
0.55	4.20E−06	1.95E−13	9.75E−15	2.77E+18	2.70E+04	0	0.915	0.5	0.00E+00
0.5	6.50E−06	3.02E−13	1.51E−14	2.52E+18	3.80E+04	0	0.915	0.45	0.00E+00
0.45	1.20E−05	5.57E−13	2.79E−14	2.27E+18	6.32E+04	0	0.915	0.4	0.00E+00
0.4	2.00E−05	9.29E−13	4.64E−14	2.02E+18	9.36E+04	0	0.915	0.3	0.00E+00
								TOTAL:	1.95E+04

Table 2 Expected star camera rate for a zero (apparent) visual magnitude, G2 class star.

Wavelength (micron)	Watts/cm2 micron	W/micron	W over (50 nm) band	Mean # photons/W	Photons/s over band	Filter B+W 090 and lens	Window trans.	CCD QE	CCD electrons/s
1	1.51E−12	4.92E−11	2.46E−12	5.04E+18	1.24E+07	0.46	0.918	0.06	3.14E+05
0.95	1.70E−12	5.51E−11	2.76E−12	4.79E+18	1.32E+07	0.51	0.918	0.1	6.18E+05
0.9	1.90E−12	6.18E−11	3.09E−12	4.54E+18	1.40E+07	0.56	0.918	0.2	1.44E+06
0.85	2.13E−12	6.92E−11	3.46E−12	4.28E+18	1.48E+07	0.64	0.917	0.3	2.61E+06
0.8	2.38E−12	7.73E−11	3.87E−12	4.03E+18	1.56E+07	0.73	0.917	0.32	3.34E+06
0.75	2.65E−12	8.60E−11	4.30E−12	3.78E+18	1.63E+07	0.79	0.917	0.47	5.54E+06
0.7	2.93E−12	9.51E−11	4.75E−12	3.53E+18	1.68E+07	0.84	0.917	0.51	6.59E+06
0.65	3.20E−12	1.04E−10	5.20E−12	3.28E+18	1.70E+07	0.84	0.916	0.6	7.87E+06
0.6	3.45E−12	1.12E−10	5.61E−12	3.02E+18	1.70E+07	0.45	0.916	0.6	4.19E+06
0.55	3.64E−12	1.18E−10	5.91E−12	2.77E+18	1.64E+07	0	0.915	0.5	0.00E+00
0.5	3.71E−12	1.21E−10	6.03E−12	2.52E+18	1.52E+07	0	0.915	0.45	0.00E+00
0.45	3.61E−12	1.17E−10	5.85E−12	2.27E+18	1.33E+07	0	0.915	0.4	0.00E+00
0.4	3.25E−12	1.05E−10	5.27E−12	2.02E+18	1.06E+07	0	0.915	0.3	0.00E+00
								TOTAL:	3.25E+07

find and identify the stars in the resulting images. In the process, we found that we could relax our identification criteria to require that at least one pixel per star image be at least five sigma above the background count level, and the entire imaged object count be at least four times that much. While this produced a few spurious, unidentified objects in each image, these were easily rejected by the identification software, and the results produced more valid objects than the earlier criteria.

Table 3 shows the results of these tests. The trend is for the number of stars identified to decrease as the filter cut-on wavelength moves further into the red. Note, however, that this conclusion is true only because of our requirement that the integration be fixed at 0.25 sec. In general, the background is falling faster at longer wavelengths than the star counts, so for a fixed number of total counts, say to some predetermined fraction of the total CCD well depth, operating at the longest wavelengths would give the best sensitivity. Nevertheless, for our fixed integration time requirement the B+W 090 filter, which transmits above $\sim 0.6\ \mu$m, provides the greatest sensitivity. Note that if we remove the filter altogether, the star brightness, averaged over all the stars found, increases by a factor of ~ 1.7 (compared with the 090 filter case), whereas the background increases by a factor of 5. This results in a net loss of sensitivity. Finally, the backgrounds are given here in electrons per pixel, rather than converted CCD counts. For a well depth of 40,000 electrons and 12-bit analog-to-digital conversion, the conversion factor is 9.77 electrons per digital count.

4 Flight Performance

Figure 4 shows the HERO payload being assembled in one of the National Scientific Balloon Facility hangars in Fort Sumner, New Mexico. Visible on the right of the payload is the vertical white tube of the star camera baffle surrounded by the white composite tubes of the x-ray mirror's optical bench. Below the baffle is a black pressurized canister housing containing the camera and the optics.

The payload was launched and flown twice, once in the fall of 2000, and once in the spring of 2001. The first flight launched at about 14:00 UT on 19 September 2000, and reached float altitude shortly after 17:00 UT. The first daytime star images, of the Cygnus X-1 region, were taken in the late afternoon that day. These were followed by daytime images of the Crab Nebula region the next morning. The second flight was launched at about 16:30 UT on 23 May 2001, and reached float altitude shortly after 18:15 UT. The

Table 3 Number of stars identified by the flight software in test images of the Crab field for various optical filters.

Filter	Cut-on (50%) (micron)	Integration time (sec)	Model background (electrons/pixel)	Number of stars found	Number of stars identified
None	—	0.25	3.3×10^4	9	5
B+W 090	0.59	0.25	6.3×10^3	13	9
B+W 091	0.63	0.25	4.1×10^3	9	8
B+W 092	0.69	0.25	2.4×10^3	9	6
Tiffen 87	0.8	0.25	5.9×10^2	8	6

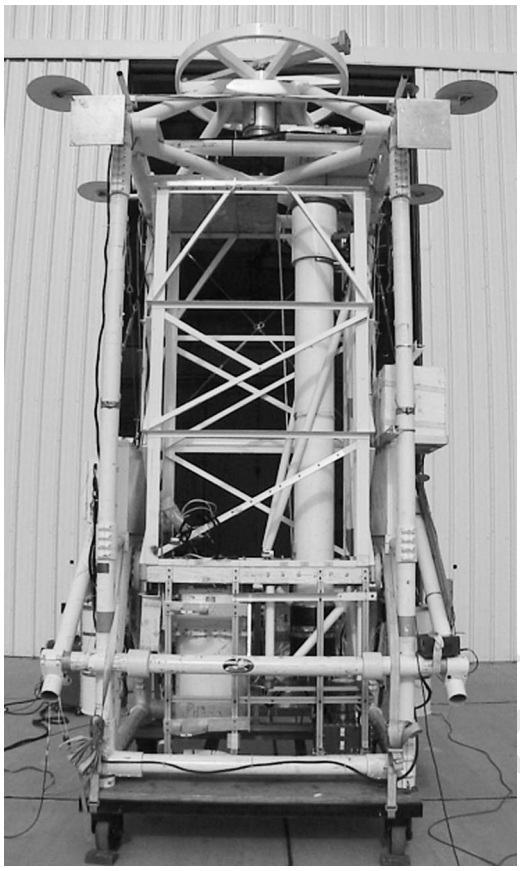

Fig. 4 The HERO payload being integrated in Fort Sumner, New Mexico. The vertical white star camera baffle tube is visible at right against the dark sky, inside the angled white tubes of the x-ray telescope optical bench.

first long-term tracking was on the Crab Nebula region later in the afternoon. A plot comparing the observed and MODTRAN-modeled backgrounds (in CCD counts per second) at several points during these daylight observations is shown in Fig. 5. Details of the illumination geometry and altitude at the times the data in the plot were taken and simulated are given in Table 4.

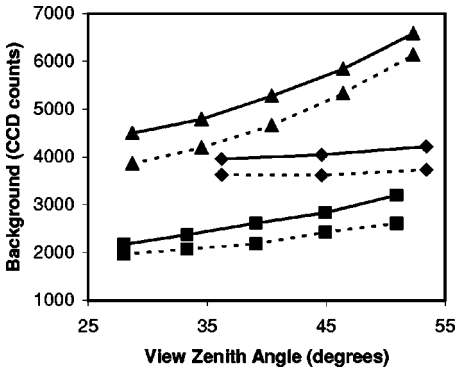

Fig. 5 Comparison of simulated and observed daytime flight backgrounds as functions of view zenith angle. Solid lines are observations; dashed lines are simulations. Diamonds are Cyg X-1 backgrounds on 19 September 2000, squares are Crab backgrounds on 20 September 2000, and triangles are Crab backgrounds on 24 May 2001.

It is evident from Fig. 5 that the shapes of the modeled data, for the most part, agree very well with the observed data, but the absolute values are slightly low. In each case, the ratio of observed to expected is very nearly 1.13. Our previous simulations in Fig. 2 imply that a very tiny amount of aerosol pollutants in the atmosphere could explain all these observations, as could scattering of the background in the optics or from dust on the glass surfaces in the optical path.

In addition, we studied the stars identified by the onboard aspect system for representative 0.25-sec exposures from the second Cyg X-1 observation and the last Crab observation. In the Cyg X-1 field, 19 stars were detected and identified by the tracking software, and for the Crab field, 11 stars were identified. For these observations, our model would have predicted limiting visual magnitudes of 9.2 and 9.7, respectively, using the measured background. The faintest stars seen in practice are 8.61 and 8.77 visual magnitude, respectively. An analysis of all Hipparcos catalog stars present in the camera fields reveals that, for the Crab observation, all the stars down to eighth magnitude and half of the stars from 8 to 8.5 were detected in the daytime. A similar analysis for the Cyg X-1 field returns all the catalog stars brighter than 7.5 magnitude, half the stars from 7.5 to 8.0, one third of the stars from 8 to 8.5, and 5 out of the 25 stars between 8.5 and ninth magnitude.

5 Discussion

It is obvious that for the two daytime star fields viewed, there were more than enough stars to obtain an accurate pointing solution, even though we did not reach our predicted magnitude limit. Both of these fields are, however, in the galactic plane and the Cygnus region in particular is very rich in bright stars. For extragalactic x-ray sources, such as the quasar 3C273, which is far out of the galactic plane (64 deg), the situation is quite different. At midafternoon on 19 September there would be only two stars brighter than eighth magnitude in the camera field. There would be, however, eight stars brighter than ninth magnitude. Therefore, it is very important that the camera achieves close to its theoretical sensitivity limit to provide fine aspect information for all star fields.

A simple comparison of achieved visual magnitude versus predicted is misleading, as it does not take into account the spectral type of each star. We are operating in the red region, but are comparing the visual magnitudes of the field stars. All stars cooler than the G2 spectral type used in the calculation will have more counts in our waveband than expected from the model. Conversely, all hotter stars will have fewer counts. Figure 6(a) shows the ratio of observed to expected CCD counts as a function of visual magnitude for the Cygnus field. As we go to fainter magnitudes we are obviously seeing cooler stars. This is only a selection effect, as these are the only ones in our band with enough excess counts to stand out over the background. Figure 6(b) depicts the same ratio, but now the expected counts factor in the spectral type of each star to derive an expected count in our operating band for the given visual magnitude (but ignoring star variability). Now we see the stars cluster more, and seem to be closer to the line where the observed CCD counts equal the expected values.

Table 4 Observation data of the observed and simulated backgrounds shown in Fig. 5.

Object	Date	Time (UT)	Altitude (m)	Exposure (sec)	VZA (deg)	SZA (deg)
Cyg X-1	9/19/2000	22:45:48	38234	0.25	53.4	64.622
Cyg X-1	9/19/2000	23:15:00	37801	0.25	44.6	70.351
Cyg X-1	9/19/2000	23:58:38	36692	0.25	36.2	78.885
Crab	9/20/2000	14:31:02	39540	0.25	28	72.01
Crab	9/20/2000	15:00:01	39741	0.25	33.3	66.632
Crab	9/20/2000	15:30:02	39617	0.125	39.1	61.186
Crab	9/20/2000	15:59:52	39599	0.125	44.9	56.024
Crab	9/20/2000	16:30:02	39628	0.125	50.9	51.147
Crab	5/23/2001	22:31:07	38812	0.25	28.7	47.811
Crab	5/23/2001	23:00:00	38533	0.5	34.5	53.769
Crab	5/23/2001	23:30:02	28350	0.5	40.4	59.736
Crab	5/23/2001	23:59:59	38175	0.5	46.4	65.666
Crab	5/24/2001	0:29:58	38008	0.5	52.3	71.482

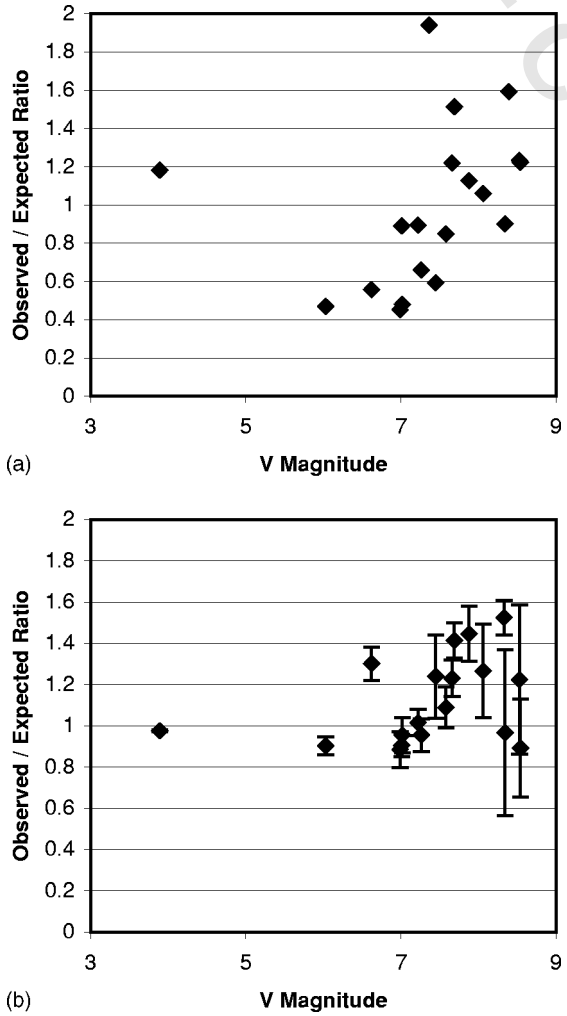

Fig. 6 Ratio of observed to expected CCD counts averaged over several daytime Cyg X-1 fields taken around 22:46 UT on 19 September 2000. In (a) at left, the expected counts assume a sun-like spectrum for all stars, but in (b) at right, the expected counts take into account the spectral type of each star.

Ideally, the plot should show a correlation with an observed/expected ratio of 1, implying that we observe exactly what we predict. Realistically, we expect there to be small light losses due to transmittances and quantum efficiency losses that are unknown and cannot be modeled, giving us an observed/expected ratio of close to but less than 1. However, the ratio shown in Fig. 6 is greater than this for most of the stars in the field. We believe this to be an artifact of the uneven shape of the daytime background, which is ~10% higher in the center than at the edges. Figures 7(a) and 7(b) demonstrate similar analysis averaged over several nighttime exposures of the same field. In these fields, the background is much lower and statistically flat across the field, the errors in the star counts are lower, and the stars seem to show an observed/expected ratio of about 0.7, which is low, but in the right direction for additional light losses such as scattering, or lower-than-expected performance of the CCD, which we did not model. Stars in this plot that have a greater ratio than 0.7 seem to have either a B-V ratio that indicates significant interstellar extinction reddening, or else are noted as variable in the catalog, and thus can be expected to differ significantly from the expected average brightness given in the catalog.

Figures 6 and 7 show that we can predict the counts from a given star with reasonable precision; however, they do not explain why we did not reach the magnitude limit we predicted in Sec. 3. To explain this, we need to look more closely at the image analysis algorithm and the distribution of light seen in each star image. Our limiting magnitude prediction relied on the assumption that 100% of the flux from a single star lay within a one-pixel radius of the center of the image, which is reasonable if the lens produces images no larger than three times the diffraction limit, as discussed in Sec. 2 before.

The actual ground and flight performance of the lens and camera, however, did not deliver sufficiently compact star images over the effective observing spectrum. As shown in Fig. 8, the images of three bright stars taken both from the ground and from the flight show a much broader distribution in which only 20 to 30% of the flux lies within one-pixel radius of the image center. This implies, at best, a

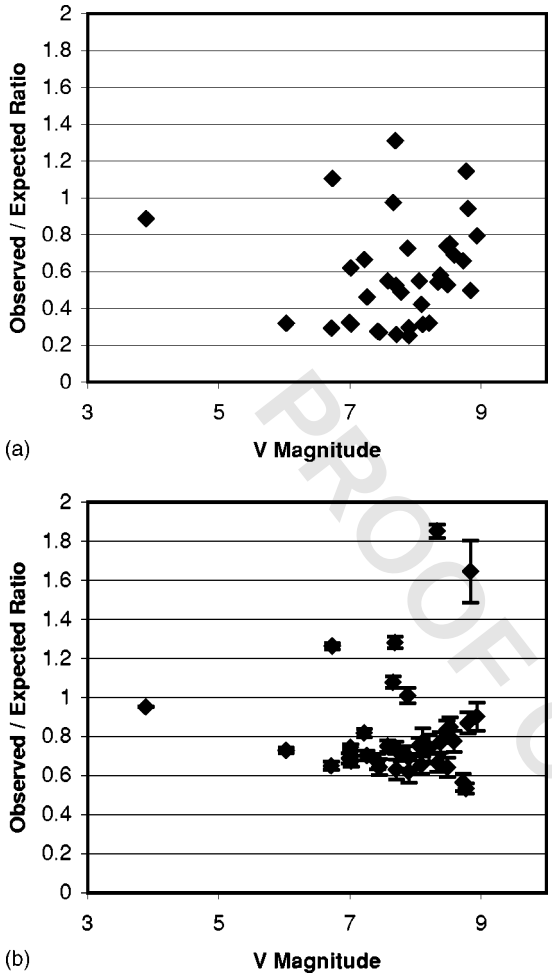

Fig. 7 Ratio of observed to expected CCD counts averaged over several nighttime Cyg X-1 fields taken around 5:48 UT on 20 September 2000. In (a) at left, the expected counts assume a sun-like spectrum for all stars, but in (b) at right, the expected counts take into account the spectral type of each star.

factor of 3 increase in the minimum detectable flux, as a star that could give at least one five-sigma pixel with an ideal flux distribution must be three times brighter to give at least one five-sigma pixel with the observed flux distribution shown in Fig. 8. A factor of 3 in brightness corresponds to a difference of 1.2 magnitudes. Thus, we should correct our predictions of the daylight magnitude limit for a G2 star from ~9 to ~7.8. This corresponds well with what we observed during the flight, as discussed before in Sec. 4. Note also that this broader distribution requires a broader collecting area in the image analysis software, which increases the noise and any systematic errors due to background subtraction.

We suspect that the cause of the broad flux distribution in our images was due to chromatic aberration. The lens, being a commercial camera lens, was designed primarily for photography in visible light, not for broadband observations across the red and near infrared, despite being labeled as low dispersion and for use in near-infrared photography. Thus, significant chromatic aberration across our wavelength band seems likely.

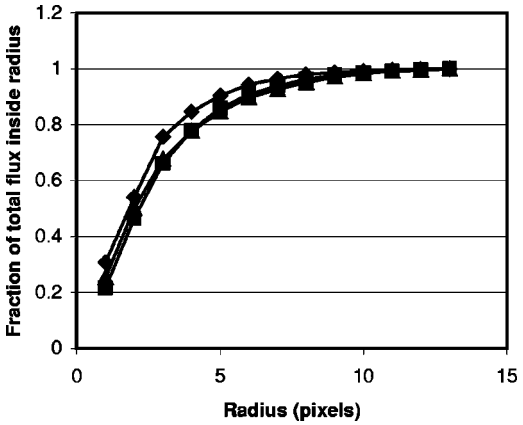

Fig. 8 Distribution of flux seen in the bright stars of three different fields. The Zeta Tauri data (diamonds) are from flight images of the Crab taken on 20 September 2000, the Eta Cygni data (squares) are from flight images of Cyg X-1 taken on 19 September 2000, and the Polaris data (triangles) are from images taken from the ground in Huntsville, Alabama on 23 March 2000.

To demonstrate this, we took two series of images of the Polaris star field from the ground at Huntsville, Alabama, on the night of 23 March 2000. In the first series, we refocused the camera for each filter, effectively giving us the focus position as a function of filter cut-on wavelength (see Table 3). The data from this series are shown in Fig. 9. In the second series, we focused the camera with no filter (which is very nearly the same as focusing with the 090 filter), taking several images with various filters without refocusing the camera. This provides a means of displaying the contribution of the various wavelengths to the size and shape of the flux distribution of each star image. The data from this series of images are shown in Fig. 10.

Figure 9 clearly shows that longer wavelengths are brought to focus closer to the lens than wavelengths of light across the visible spectrum, and that this effect becomes more significant at wavelengths greater than 650 nm. In addition, Fig. 10 shows that when the lens is focused for visible light, the broad wings of the flux distribution are due to light from longer wavelengths. Thus, it is obvious

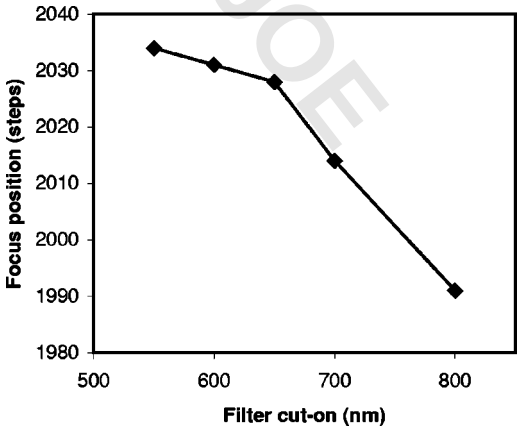

Fig. 9 Star camera focus position as a function of filter cut-on wavelength for the Polaris field on the night of 23 March 2000 from the ground at Huntsville, Alabama. Focus position is given in stepper motor steps (see text.)

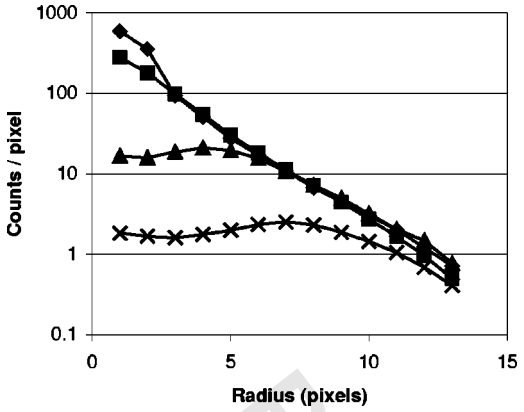

Fig. 10 Image profiles of Polaris through filters of various cut-on wavelengths (see Table 3). The diamonds are from the image taken without any filter, the squares from the B+W 090 filter image, the triangles from the B+W 092 filter image, and the crosses from the Tiffen 87 filter image.

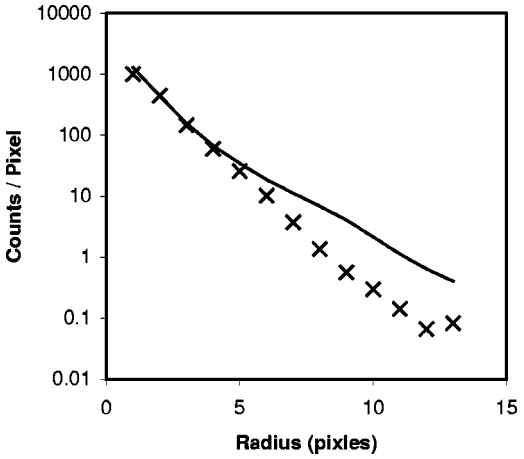

Fig. 11 Comparison of Polaris image profiles using two separate filters. The solid line is the average profile from 16 images taken with the B+W 090 red filter, and the crosses are the average profile from 16 images taken with the combination of the Tiffen 15 yellow filter and the Heliopan Digital UV/IR cut-off filter. All data were taken from the ground at Huntsville on 27 September 2001.

that the longitudinal chromatic aberration of this lens is the cause of the broad stellar images we observed, and therefore is the chief cause of the reduction of sensitivity during daytime observations.

As discussed previously, our current low-cost camera and lens system (about $11,000 for the camera and about $800 for the lens) is perfectly adequate for many star fields near the galactic plane, and can be used without modification to guide a balloon experiment in those cases. However, to reach any arbitrary field at any galactic latitude, we require a limiting magnitude of 9 or greater. Our current camera, lens, and filter arrangement provides adequate flux to accomplish this, but does not focus that flux tightly enough to allow unambiguous detection of stars below about eighth magnitude during the day. This leaves us with two choices: 1. keep the current lens and camera, but find a new filter wavelength range closer to the visible that will provide a sharper focus without greatly increasing the background, or 2. find or build a lens that does not significantly disperse light from 600 to 1000 nm. The first option is considerably less expensive and time consuming than the second, so we have chosen to investigate the first.

We chose to use the wavelength range from 550 to 750 nm because of the cost and availability of the two filters used to create it: a Tiffen 15 deep yellow filter that passes light longer than 550 nm, and a Heliopan ES72 Digital UV/IR cut-off filter that passes light from 300 to 750 nm. Our models showed that the sky background should be about 23% greater than that seen with the current filter, and the flux from a star of solar-type spectrum would only be about 70% of that seen with our current filter. We predicted that even though the total flux would be reduced, a sufficiently improved focus could actually produce more flux in the central pixels, making fainter stars detectable. We imaged Polaris on the evening of 27 September 2001 from the ground in Huntsville, taking 16 images with our current filter and 16 images with the new filter pair. The averaged star profiles are shown in Fig. 11. Clearly, Fig. 11 shows that while the new filter combination does offer a narrower star image than our current filter, it does not produce a brighter central core than the current filter. The focus improvement across this new filter band is not enough to offset the loss of total flux compared to the original filter band.

It appears that this approach will not be productive for reaching fainter guide stars. To focus more sharply, the system requires a filter set with a bandpass farther toward the blue. However, as the operating bandpass moves toward the blue, the background counts rise more rapidly than the star counts. In fact, if we limit ourselves to bands with wavelength shorter than 650 nm, our models predict that it is not possible to reach fainter than eighth magnitude, even with perfect focus. In addition, at high galactic latitudes, the stellar population tends to be dominated by older, redder stars, such that systems operating in the bluer portion of the visible spectrum must reach 0.5 to 1 magnitudes fainter to see the same number of stars per square degree as a system operating in the red.

It seems that the only means of reaching fainter stars in the daytime is a new lens that will not significantly disperse light in our wavelength region of interest. An in-house optics team at MSFC designed an optical system to deliver a 180-mm focal length, an f/2.8 speed, a 2-deg field of view, and a spot size of 6.8 μm containing 84% of the energy. The system contains six lens elements, and has an estimated fabrication cost on the order of tens of thousands of dollars. Using the background model for the Crab Nebula field at 0:30 UT on 23 May 2000, the highest we observed in flight, and our standard stellar flux model, we calculated the magnitude limits for our current lens and for this new lens to obtain the data in Table 5. The current lens parameters appear to be that 25% of a star's flux lies within one-pixel radius of the center, and that the operational wavelength band is 600 to 1000 nm. The new lens specification is for 84% of the flux to fall within a circle of one-pixel (6.8 μm) radius, across the operational wavelength band of 600 to 750 nm. Both assume that the stellar flux within a one-pixel radius must be 20 sigma above the background. Clearly, during the daytime, this new lens will detect stars nearly a magnitude fainter than our current system, which should produce enough star images to provide

Table 5 Comparison of daytime stellar magnitude limit of the current camera and the new theoretical lens design for three representative star temperatures.

Star temp (K)	Current system magnitude limit	Proposed system magnitude limit
9000	7.0	8.1
5780	7.3	8.4
3600	8.0	8.9

aspect information for any arbitrary star field in the sky.

All our simulations have assumed a flight altitude of 40 km, and our flight results were obtained at nearly the same altitude; however, not all balloon experiments target or achieve this altitude. To get a rough idea of the sensitivity of the camera at other float altitudes, we have taken a nighttime image of the Crab Nebula region obtained during our flight and added in MODTRAN model daytime backgrounds representative of various altitudes. For each image, we then applied the flight star-tracking software to obtain the number of identified stars that could be used to derive aspect information. The background models do not take into account the fact that the observed backgrounds at our float altitude were slightly higher than those predicted by the model, but the star tracking does account for the fact that the observed star images generally do not include as many counts as expected, because we used an actual flight image of the sky. The results are given in Table 6, and show that the current system could track the Crab Nebula field down to an altitude of 28 km.

6 Conclusion

We have designed and flown a star camera capable of resolving at least eighth magnitude stars in the daytime at a float altitude of 40 km, which is adequately sensitive to detect enough stars to provide high resolution aspect information for many targets near the galactic plane. The camera design was optimized using a model of the daytime sky brightness at float altitudes coupled with calculations of expected star counts. In flight, the observed background was very close to that predicted and a large number of daytime stars (11 and 19) were detected in the two bright star fields viewed. Subsequent ground analysis revealed that the limiting sensitivity was roughly 1 magnitude poorer than expected, given the measured background, and this was traced to significant chromatic aberration at wavelengths beyond ~650 nm. If used with a custom lens that focuses all the light of wavelength 600 to 750 nm into a single pixel radius, the camera can reach a limiting daylight magnitude of almost ninth magnitude at an altitude of 40 km, which would be adequate for detecting sufficient stars to provide fine aspect information for any arbitrary star field.

Table 6 Estimate of daytime background and star camera performance at various altitudes.

Altitude (km/kft)	Background/pixel (CCD counts/0.25 sec)	Number of stars identified
39.6/130	563	11
38.1/125	701	10
36.6/120	878	10
35.0/115	1068	9
33.5/110	1332	6
32.0/105	1654	6
30.5/100	2086	5
27.4/90	3249	4

Acknowledgments

We are grateful to Helen Cole of MSFC's optics division, Tim Blackwell of the University of Alabama at Huntsville, and Blair Unger of William Jewell College for measuring the transmittance of various filters and lenses for use in our models. We also want to thank John Hraba and Ken Pitalo, also of MSFC's optics division, for designing a next-generation custom lens and for providing an estimate of the fabrication cost.

References

1. W. W. Craig, R. McLean, and C. J. Hailey, ''Sub arcminute pointing from a Balloon borne platform,'' *Proc. SPIE* **3365**, 87–97 (1998).
2. B. D. Ramsey, C. D. Alexander, J. A. Apple, R. A. Austin, C. M. Benson, K. L. Dietz, R. F. Elsner, D. Engelhaupt, J. J. Kolodziejczak, S. L. O'Dell, C. O. Speegle, D. A. Swartz, M. C. Weisskopf, and G. Zirnstein, ''HERO: High Energy Replicated Optics for a hard-x-ray balloon payload,'' *Proc. SPIE* **4138**, 147–153 (2000).
3. C. Alexander, W. Swift, K. Ghosh, and B. D. Ramsey, ''Design of a day/night star camera system,'' *Proc. SPIE* **3779**, 47–54 (1999).
4. See http://astro.estec.esa.nl/Hipparcos/.
5. See http://spider.ipac.caltech.edu/staff/jarrett/num_mod/num_mod.html.

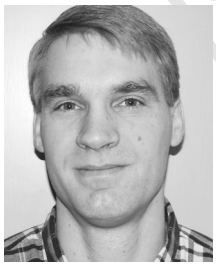

Kurt L. Dietz received his BS degree in physics and astronomy from the University of Arizona in 1988. He has worked at the Marshall Space Flight Center from 1989 to the present as a computer scientist. In addition to designing and implementing the star image-based software flown on the HERO mission, he has also been involved with data analysis and imaging in both x-ray and infrared astronomy and led the programming effort to model the effects of high-energy photons on the Chandra X-Ray Observatory detector backgrounds. Currently, he focuses on designing and implementing experiment control programs for both embedded and ground systems in the areas of balloon-borne x-ray astronomy and aircraft-based atmospheric microwave radiometry.

Brian D. Ramsey received his MSc in physics and PhD in astrophysics from the University of Birmingham, England, in 1975 and 1978, respectively. After a postdoctoral fellowship in England he moved to the Marshall Space Flight Center in 1983 and now works in the space science department. He is author or coauthor of 125 papers in astronomy and instrumentation and is currently responsible for the development of x-ray optics and detectors.

Cheryl D. Alexander received her BS and MS in electrical engineering with an emphasis in optics from the University of Alabama in Huntsville in 1993 and 1994, respectively. She began working at NASA's Marshall Space Flight Center (MSFC) as a cooperative education student in 1990, and joined the center full-time upon completion of her Masters degree in 1994. She has worked in MSFC's Program Development Office on proposed lunar and space station projects, in the Flight Projects Office on a space-based tethered deployer system, and in the Optics Division in the test and development of x-ray and binary optical systems. She has worked for the past six years in the x-ray astronomy group of the Space Science Department, where she supports the development and testing of x-ray astronomy telescopes and support instrumentation.

Jeff A. Apple received his BSEE degree from the Tennessee Technological University in 1986. He has worked at the Marshall Space Flight Center from 1986 to present as a senior engineer responsible for design and development of electronic and mechanical systems in support of research activities in the Science Directorate. He personally specializes in low noise analog circuit design and the use of commercial off the shelf (COTS) equipment to build custom data acquisition systems used both in the laboratory and in the field under extreme environmental conditions.

Kajal K. Ghosh received his PhD in astrophysics from Calcutta University, India, in 1983, where he was a Research Scholar between 1977 and 1981. He served as a lecturer for Calcutta University from 1981 to 1984 teaching undergraduate students. He was a Resident Astronomer at the Vainu Bappu Observatory, Indian Institute of Astrophysics, India, from 1984 to 1998. He served as a visiting scientist at nine institutions in six different countries. Most recently, he has worked as the Senior Resident Research Associate of the National Research Council, in the x-ray astronomy group at NASA's Marshall Space Flight Center. Presently he is working as the scientist of the USRA. His research fields of interests are the multiwavelength studies of Be stars, supernovae, x-ray binaries, normal and starburst galaxies, and active galactic nuclei.

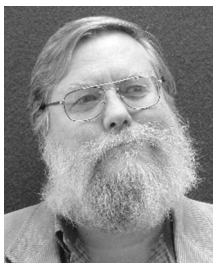

Wesley R. Swift earned his MS (physics) at the University of Alabama in Huntsville (UAH) and was employed by the Optical Aeronomy Laboratory (OAL) at UAH from 1986 to 2001. NASA/OAL projects include the ISUS, a balloon instrument; the ISO, which flew on ATLAS I; and the UVI on the POLAR satellite. For the NSF, he operated the ISO at McDonald Observatory, where he developed all required data reduction software, and designed, built, and developed the Optimized Airglow Spectrometric Imaging System. He designed the hardware and software for a day/night CCD astroguider for a NASA x-ray balloon telescope. In 2000 he calibrated the ISO data for archive at NSSDC and wrote a GUI-based analysis program for the data. He is presently employed by Raytheon and is located at MSFC/ED44 in the Space Environments group. His duties include the adaptation of space science models and data as space weather engineering applications.